

Eccentric Disks With Self-Gravity

YORAM LITHWICK,^{1,2} EUGENE CHIANG,^{3,4} LEON MIKULINSKY,⁵ AND ZHENBANG YU⁶

¹*Department of Physics & Astronomy, Northwestern University, Evanston, IL 60202, USA*

²*Center for Interdisciplinary Exploration & Research in Astrophysics (CIERA), Evanston, IL 60202, USA*

³*Department of Astronomy, Theoretical Astrophysics Center, and Center for Integrative Planetary Science, University of California Berkeley, Berkeley, CA 94720-3411, USA*

⁴*Department of Earth and Planetary Science, University of California Berkeley, Berkeley, CA 94720-4767, USA*

⁵*Department of Mathematics, 970 Evans Hall, University of California Berkeley, Berkeley, CA 94720-3840*

⁶*Department of Physics, 366 Physics North MC 3700, University of California Berkeley, Berkeley, CA 94720-7300*

ABSTRACT

Can a disk orbiting a central body be eccentric, when the disk feels its own self-gravity and is pressureless? Contradictory answers appear in the literature. We show that to linear order in eccentricity such a disk *can* be eccentric, but only if it has a sharply truncated edge: the surface density Σ must vanish at the edge, and the Σ profile must be sufficiently steep at the point where it vanishes. If either requirement is violated, an eccentric disturbance leaks out of the bulk of the disk into the low density edge region, and cannot return. An edge where Σ asymptotes to zero but never vanishes, as is often assumed for astrophysical disks, is insufficiently sharp. Similar results were shown by Hunter & Toomre (1969) for galactic warps. We demonstrate these results in three ways: by solving the eigenvalue equation for the eccentricity profile; by solving the initial value problem; and by analyzing a new and simple dispersion relation that is valid for any wavenumber, unlike WKB. As a byproduct, we show that softening the self-gravitational potential is not needed to model a flat disk, and we develop a softening-free algorithm to model the disk's Laplace-Lagrange-like equations. The algorithm is easy to implement and is more accurate than softening-based methods at a given resolution by many orders of magnitude.

1. INTRODUCTION

We consider astrophysical disks that orbit a central body, and that are sufficiently massive that self-gravity is important. Examples include planetary rings, protoplanetary disks, and disks of stars in galactic nuclei. Many such disks are observed to be eccentric. Understanding why and how such disks are eccentric should teach us about their internal physics (e.g. gravity, pressure, viscosity), and about external perturbers, such as planets in protoplanetary disks, moons in planetary rings, and the galactic tidal potential of galactic nuclei.

Test particles orbit a central point mass along non-precessing Keplerian ellipses. A disk of test particles on nested ellipses remains eccentric forever. But for a disk of massive particles the ellipses interact, forcing one another to precess. Differential precession would rapidly wipe out an eccentricity profile. Nonetheless, it is plausible that particular arrangements of eccentricity and mass can be made to precess uniformly, leading to a long-lived eccentricity. Goldreich & Tremaine (1979a) worked out possible such profiles for the eccentric and radially narrow Uranian rings. Our goal here is to ex-

pand the class of such rigidly precessing solutions and understand more generally their properties.

Sridhar et al. (1999) solved the problem of an eccentric and radially extended disk of massive particles, with the ultimate goal of explaining double nuclei of galaxies (Tremaine 1995). They employed Laplace-Lagrange theory, in which uniformly precessing eccentricity patterns emerge as solutions of an eigenfunction problem (Murray & Dermott 1999). They successfully found solutions, as may have been expected from Laplace-Lagrange theory.

Tremaine (2001) investigated self-gravitating eccentric disks by solving the fluid equations rather than using Laplace-Lagrange theory. While he found that narrow rings can support eccentricity modes supported purely by self-gravity, he concluded that extended disks cannot, in contradiction to Sridhar et al. (1999). We will resolve this disagreement as part of our study. Tremaine (2001) also explored the effect of softening gravity as a model for pressure, and developed a simple graphical technique for explaining the properties of the eigensolutions, which we shall adapt below.

Many later papers studied eccentric self-gravitating disks, sometimes including pressure or external perturbations such as planets (e.g. Papaloizou 2002; Touma 2002; Hahn 2003; Silsbee & Rafikov 2015; Teyssandier & Ogilvie 2016; Davydenkova & Rafikov 2018; Sefilian & Rafikov 2019; Teyssandier & Lai 2019). Lee et al. (2019a, written with one of us) found that extended disks with both pressure and self-gravity do support eccentric modes. But as the strength of self-gravity is increased relative to pressure, the eccentric modes become increasingly pathological, in the sense that their wavelengths become extremely small. This accords with Tremaine (2001)'s finding that extended self-gravitating disks cannot be eccentric, but contradicts the expectation from Laplace-Lagrange theory (Sridhar et al. 1999).

In this paper we shall show that the key factor in whether a self-gravitating disk can be eccentric is the shape of the disk's surface density profile near its edge. Other factors, such as whether the disk is extended or narrow, do not affect that conclusion.

2. MASTER EQUATION

We assume throughout that the disk is two-dimensional, that the only operative forces are self-gravity and gravity from the central mass, and that eccentricities are governed by the linear secular equations. We discuss additional effects in Section 7.

The linear secular equation of motion for an orbiting body that is perturbed by another is, from Murray & Dermott (1999)

$$\dot{z} = i \left(\frac{G}{M_*} \right)^{1/2} \frac{m'}{4aa'^{1/2}} \left(\alpha^{3/2} b_{3/2}^{(1)}(\alpha) z - \alpha^{3/2} b_{3/2}^{(2)}(\alpha) z' \right) (1)$$

where z is the perturbed body's complex eccentricity,

$$z = ee^{i\varpi} ; \quad (2)$$

a is the perturbed body's semimajor axis; z' and a' are the corresponding quantities for the perturber; m' is the perturber's mass; M_* is the central mass; the $b_s^{(m)}$'s are Laplace coefficients; and α is the ratio of semimajor axes. When written in the above form, one need not specify whether $\alpha = a/a'$ or a'/a because the product $\alpha^s b_s^{(j)}(\alpha)$ is unchanged when $\alpha \rightarrow 1/\alpha$. Note that our primed variables refer to the perturber, in contrast to Murray & Dermott's primed variables which refer to the exterior body.

In what follows we convert the equation of motion from discrete bodies to that of a continuous disk, and then discretize the continuum equations. That seemingly circular route will lead us to a more accurate numerical treatment than simply adopting Equation (1).

For the continuum limit of Equation (1), we consider z to be a function of a , and z' and m' to be functions of a' ; replace $m' \rightarrow 2\pi\Sigma(a')a'da'$, where $\Sigma(a)$ is the surface density profile; define the scaled surface density

$$\sigma \equiv \pi \left(\frac{Ga^3}{M_*} \right)^{1/2} \Sigma = \frac{\pi G}{\Omega} \Sigma , \quad (3)$$

which has dimensions of speed, and use that to replace $\Sigma(a')$ with $\sigma(a')$; change the independent variable from a to

$$u = \ln a , \quad (4)$$

and similarly from a' to $u' = \ln a'$; and integrate over u' . The resulting continuum equation of motion is

$$\dot{z}(u) = i \frac{1}{a(u)} \int (K_1(u' - u)z(u) - K_2(u' - u)z(u')) \sigma(u') du'$$

which we call the master equation. The two kernels are defined by

$$K_m(v) = \frac{1}{\pi} \int_0^\pi \frac{\cos m\phi d\phi}{(2 \cosh v - 2 \cos \phi)^{3/2}} \quad (5)$$

and are related to the Laplace coefficients via $K_m(v) = (1/2)\alpha^{3/2} b_{3/2}^{(m)}(\alpha)|_{\alpha=e^v}$. Note that the kernels depend only on the difference $u' - u$ (Kalnajs 1971), which will prove convenient. To cut down on brackets we adopt a shorthand for the master equation,

$$\dot{z} = i \frac{1}{a} \int (K_1 z - K_2 z') \sigma' du' , \quad (6)$$

where throughout this paper kernels without explicit arguments represent $K_m \rightarrow K_m(u' - u)$.

The two kernels are plotted in Figure 1. They are symmetric, $K_m(v) = K_m(-v)$. At $|v| \ll 1$ they diverge strongly,

$$K_1(v) \approx K_2(v) \approx \frac{1}{\pi v^2} + O(\ln |v|) . \quad (7)$$

where the $O(\ln |v|)$ term is different for the two K 's. The kernels may be expressed in terms of associated Legendre functions, elliptic integrals, or hypergeometric functions (Cohl & Tohline 1999).

The master equation conserves the angular momentum deficit

$$\text{AMD} \equiv \int |z|^2 \sigma a du , \quad (8)$$

(e.g., Teyssandier & Ogilvie 2016), which follows from the kernels' symmetry in v .

Many papers have studied equations of motion similar to the master equation, including Sridhar et al. (1999);

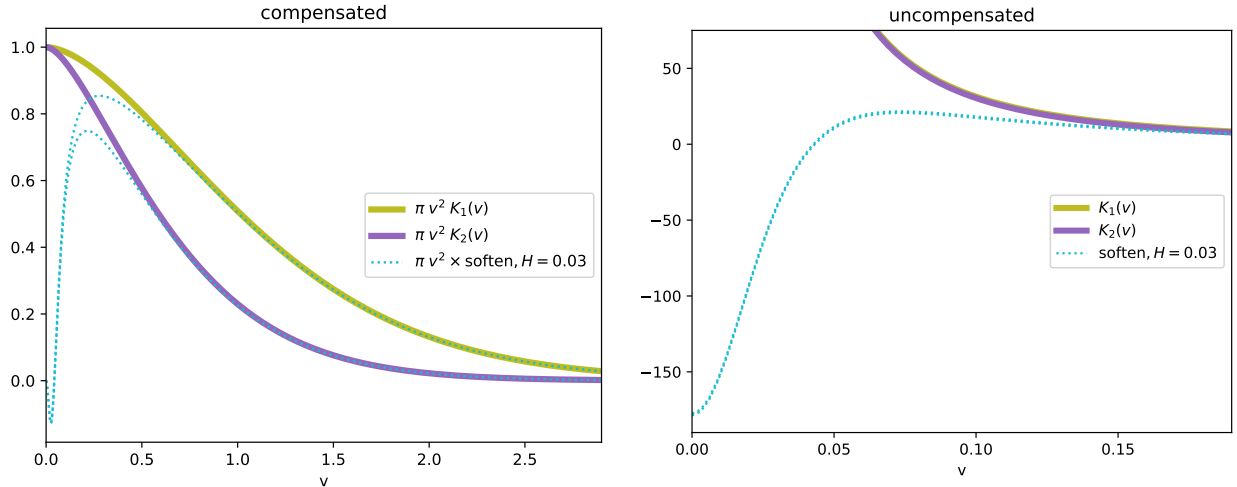


Figure 1. Kernels: The kernels are defined in Equation (5). They have a strong $1/v^2$ divergence at $|v| \ll 1$ (Equation (7)), and hence have been multiplied in the left panel by πv^2 to compensate. The blue dotted curves in the left panel are softened kernels (Hahn 2003) with the same compensation by πv^2 . The right panel shows the uncompensated kernels, with axes adjusted. The softened kernels have a rapid zero-crossing at $v \lesssim H$, and so numerical integrations that incorporate these softened kernels require extreme resolution. The reason for the rapid zero crossing is that the softened kernels must come from taking derivatives of the softened potential, rather than from directly softening K_1 and K_2 (Tremaine 2001; Sefilian & Rafikov 2019).

Tremaine (2001); Papaloizou (2002); Hahn (2003); Teysandier & Ogilvie (2016); Sefilian & Rafikov (2019) and Lee et al. (2019a).

Sridhar et al. (1999) modelled their disk as discrete bodies, using Equation (1) directly. We shall show that this approach, called Laplace-Lagrange theory, converges to the continuum solution as the number of discretizing bodies is increased. But the convergence is slow.

Tremaine (2001) derived our master equation (his Equation (42)) in a different way, by linearizing the two-dimensional fluid equations. Tremaine (2001) states that Laplace-Lagrange (L-L) theory is incorrect for a continuous disk, because it assumes eccentricities are small compared to the relative distance between rings, and that that inapplicable assumption may be rectified by softening. But the fact that the two derivations produce identical continuum equations shows that Laplace-Lagrange theory does not rely on such an extreme assumption. While L-L theory does fail for crossing orbits (e.g. for a test particle whose orbit crosses those of disk particles), it yields correct behavior for non-crossing orbits in the continuum limit, and in particular the correct (positive) precession rate for an eccentric disk.

3. DISCRETIZATION WITHOUT SOFTENING

To solve the master equation, we discretize in u . Our discretization will differ slightly from Equation (1). But that slight difference leads to faster convergence to the correct answer as the number of discretization points increases. The derivation of the discretization is in the

appendix. Here, we provide a summary. Readers uninterested in numerics may skip to the next section without loss.

The integral in Equation (6)

$$\mathcal{I}(u) \equiv \int (K_1 z - K_2 z') \sigma' du' \quad (9)$$

must be evaluated carefully. The kernels diverge sufficiently strongly at small argument ($|u - u'|$) that each of the two terms in Equation (9) is infinite. But the two infinities cancel, because as u' approaches u , then both $z' \approx z$ and $K_1 \approx K_2$ (Figure 1); or to be more precise, $K_1 - K_2 \approx O(\ln|u - u'|)$, and the integral of that difference does not diverge (see below Equation (A13)).

An elegant way to avoid the infinities is to soften the kernels, which forces the K_1 and K_2 integrals to converge separately (Tremaine 2001; Touma 2002; Hahn 2003). Example softened kernels are shown as blue dotted curves in Figure 1. As the softening length is reduced, \mathcal{I} converges to the correct answer, as shown by Sefilian & Rafikov (2019). Softening has the added benefit that it mimics what happens in a 3D disk. But softening comes with an onerous computational cost. To achieve an error of $\delta\mathcal{I}$ in an extended disk, while adequately resolving the softening scale, requires $\gtrsim 3(\mathcal{I}/\delta\mathcal{I})^2$ gridpoints per decade in a (Sefilian & Rafikov 2019). For example, for a 1% error more than 30,000 gridpoints per decade are required,⁷ which is compu-

⁷ When softened kernels are used, there are two contributions to the error $\delta\mathcal{I}$. First, softening changes the kernel, and so

tationally challenging: the eigensolution of an $N \times N$ matrix on a laptop takes around 1 second $\times (N/3000)^3$, which rapidly becomes problematic as N is increased. The memory cost also explodes.

We avoid this difficulty by avoiding softening.⁸ But we must then carefully account for the near-divergences in Equation (9). We do that in the appendix. We assume there that σ and z are intrinsically smooth functions of u ; adopt a grid in u with uniform grid-spacing Δ ; and use the values of σ and z on that grid. The result for the discretization of \mathcal{I} is given by Equation (A14). Its error is $\sim \Delta^2$. Hence to achieve a 1% error in an extended disk it suffices to take $\Delta \sim 0.1$, corresponding to ~ 20 gridpoints per decade in a .

We demonstrate the accuracy of our discretization in Figure 2. We use the power-law form of Sefilian and Rafikov,

$$\sigma = a^{-p+3/2} \quad (10)$$

$$z = a^{-q}, \quad (11)$$

and evaluate \mathcal{I} at $a = 1$ ($u = 0$). We choose the bounds on the integral to be $u' = -12, 12$. The orange and dark blue points show the fractional error $\delta\mathcal{I}/\mathcal{I}$ at different grid spacings, where the two colors are for different values of p and q . One sees that the fractional error is better than Δ^2 . The points labelled “discrete, naive” are evaluated in the same way as the corresponding discretized points, but with the factor of 1.5 in Equation (A11) changed to unity, as in Equation (A6). That nearly trivial change, which corresponds to dropping the single point with index $k = j$ (as in Laplace-Lagrange theory), makes the error much worse; but it still converges to the correct answer at small Δ .

We also compare in the figure with the result from softening. A variety of different softenings have been introduced in the literature, as summarized in Sefilian & Rafikov (2019). See also Rendon Restrepo et al. (2025), who introduce a softening that mimics Gaussian-stratified disks. We adopt, somewhat arbitrarily, the

produces an error even if the integral over the softened kernel is performed at infinite resolution. In the example presented below (Figure 2), the softening scale must be $H < 0.003$ in order to achieve a 1% error at infinite resolution. Second, there is an error due to discretizing the integral. Because of the rapid variation of the softened kernel near $v \sim 0$ (Figure 1), accurate discretization requires $\Delta \ll H$. Extrapolating Figure 9 in Sefilian & Rafikov (2019), one sees that at least 30,000 gridpoints per decade are needed to achieve 10% accuracy of the softened kernel at $H = 0.003$; to achieve a 1% error would require even more gridpoints.

⁸ Heppenheimer (1980) considers the perturbation induced by a circular disk that has a power-law surface density profile. For that case, he is able to avoid softening by computing the relevant integral analytically.

one introduced by Hahn (2003). We replace the K ’s in Equation (9) with their softened counterparts, which are provided in Table 1 of Sefilian & Rafikov (2019). Specifically, we replace $K_1(v) \rightarrow 4\alpha^{1/2}\phi_{11}|_{\alpha=e^v}$, where the ϕ_{11} is listed in that table, and $K_2(v) \rightarrow -2\alpha^{1/2}\phi_{12}|_{\alpha=e^v}$. The ϕ functions depend both on α and on a dimensionless softening length H , which is roughly analogous to our grid spacing Δ , in the sense that H sets the length-scale below which interparticle forces are modelled incorrectly (Figure 1). Using those softened K ’s, we perform the integral in \mathcal{I} numerically at infinite resolution, i.e., we ensure that the discretization scale Δ is sufficiently small that it does not affect the accuracy of the integral. The result is shown as the light blue squares in Figure 2, versus softening scale H . Comparing with the dark blue circles shows that softening performs significantly worse. As mentioned above, the performance of softening is even worse than suggested by the figure. In order to discretize the softened integral, one must use discretization $\Delta \ll H$. Hence the light blue squares in Figure 2 should be shifted to the left by the factor $H/\Delta \gg 1$ when plotted versus Δ instead of H .

4. SHARP EDGE VERSUS SOFT EDGE

The main result of this paper is that disks with sharp edges can remain eccentric, whereas those with soft edges cannot. To highlight the dichotomy, in this section we solve the master equation for two disk profiles that bracket the sharp vs. soft transition. For both profiles, the scaled surface density (Equation (3)) follows the profile

$$\sigma = (1 - a)^\gamma \quad \text{for } a < 1, \quad (12)$$

with an outer edge at $a = 1$. For the sharp profile, $\gamma = 0.5$, and for the soft, $\gamma = 1.5$. These are plotted in the top-left panel of Figure 3. The two profiles look broadly similar, but will be shown to produce dramatically different eccentricity behavior. One may imagine that Equation (12) extends to $a \rightarrow 0$. In truth, for the numerical experiments in the present section we set the inner boundary to be at $a = 0.05$ ($u = -3$), and set $\sigma = 0$ inside of that. But we will verify in Section 6 that the inner boundary plays a negligible role.

In the following, we first solve the eigenvalue problem, and then evolve in time. We turn to the theoretical explanation in Section 5.

4.1. Eigensolution

We solve the master equation (Equation (6)) by setting $z(u, t) = \hat{z}(u)e^{i\omega t}$. That produces an eigenvalue equation, with eigenvalue ω , and eigenvector \hat{z} . The discretized eigenvalue problem is derived in the appendix,

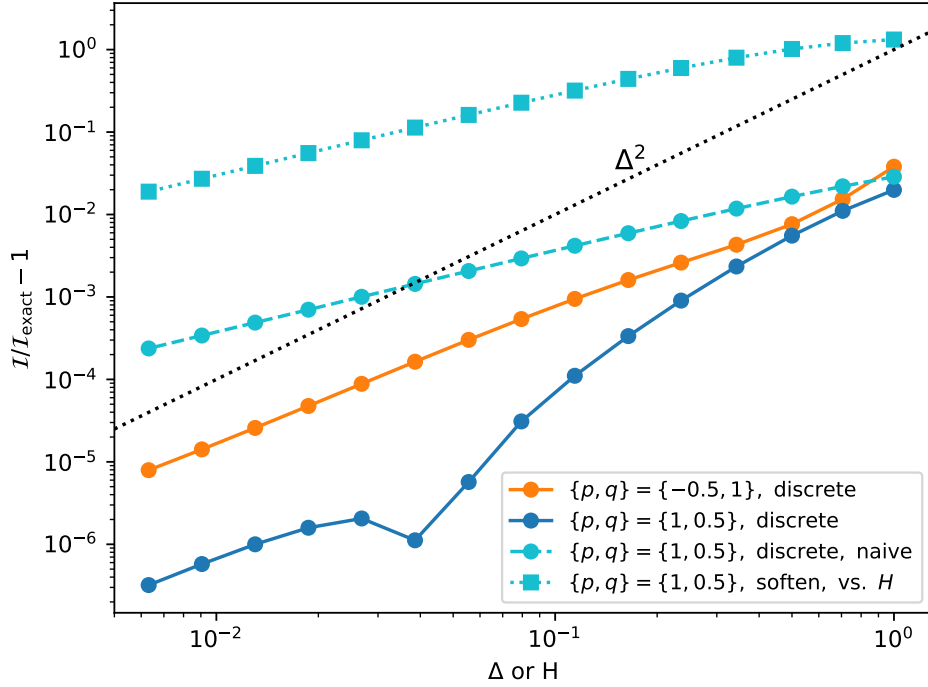


Figure 2. Comparison of Approximations to \mathcal{I} : The points connected by solid curves (orange and dark blue) show the error in the discretized approximation (Equation (A14)), versus grid spacing Δ . The error is better than Δ^2 . The light blue circles (labelled “discrete, naive”) repeat the dark blue circles, but with the factor of 1.5 in Equation (A11) changed to unity. The light blue squares (labelled “soften”) show the result with a softened kernel, integrated at infinite resolution ($\Delta \rightarrow 0$), and plotted versus H rather than Δ . This performs much worse than the dark blue circles. For a fairer comparison, the light blue squares should be discretized at $\Delta \neq 0$, and plotted versus Δ ; that would worsen the discrepancy with the dark blue circles.

and given in matrix form in Equation (A26). As shown there, the eigenvalues and eigenvectors are real-valued. The eigenvalues are positive ($\omega > 0$), which corresponds to prograde precession.

The top-right panel in Figure 3 shows the first three eigenvectors for the sharp ($\gamma = 0.5$) case, where eigenvectors are ordered by the number of nodes, or equivalently by their eigenfrequencies, which increase with node number. The eigenvectors are seen to converge with resolution: as the grid spacing is reduced from $\Delta = 0.03$ to 0.003, they hardly change.

By contrast, for the soft ($\gamma = 1.5$) profile the eigenvectors are pathological, as shown in the bottom panels of Figure 3. As Δ is decreased, they become peaked ever closer to the outer edge. We normalize our eigenvectors to have AMD=1 (Equation (A28)). Hence the shift towards the edge seen in Figure 3 reflects a shift of AMD. The eigenvectors have not converged even for $\Delta = 0.0003$. Based on the trend seen in the figure, they presumably will never converge.

A similar inference follows from the dependence of the eigenvalues on resolution (Figure 4). For the $\gamma = 0.5$ case, ω quickly converges to a fixed value as Δ decreases. But for the $\gamma = 1.5$ case, all of the modes’ frequencies

approach each other. At high resolution, the frequencies become degenerate.

4.2. Time Evolution

We consider now the time-dependent problem. We initialize the eccentricity profile as

$$z_{\text{init}} = e_{\text{init}} = e^{-(a/0.2)^4}, \quad (13)$$

i.e., purely real (nodally aligned), with constant eccentricity at $a \lesssim 0.2$, and with a rapid transition to circularity for $a \gtrsim 0.2$. We then evolve z forward in time by numerically integrating the discretized equation of motion (Equation (A23)), with grid spacing $\Delta = 0.01$. The results are shown in Figure 5, where we plot profiles of $\text{Real}[z]$ at successive times, displaced vertically. In the $\gamma = 0.5$ disk, the initial eccentric disturbance travels towards the outer edge, where it reflects and then travels inwards. But in the $\gamma = 1.5$ disk, the disturbance stalls. It produces increasingly rapid spatial variations before it can reach the outer edge. At some point, the disturbance will become nonlinear, invalidating our assumption of linearity in e . To understand what happens next would require solving the nonlinear equations of motion, which we do not attempt in this paper.

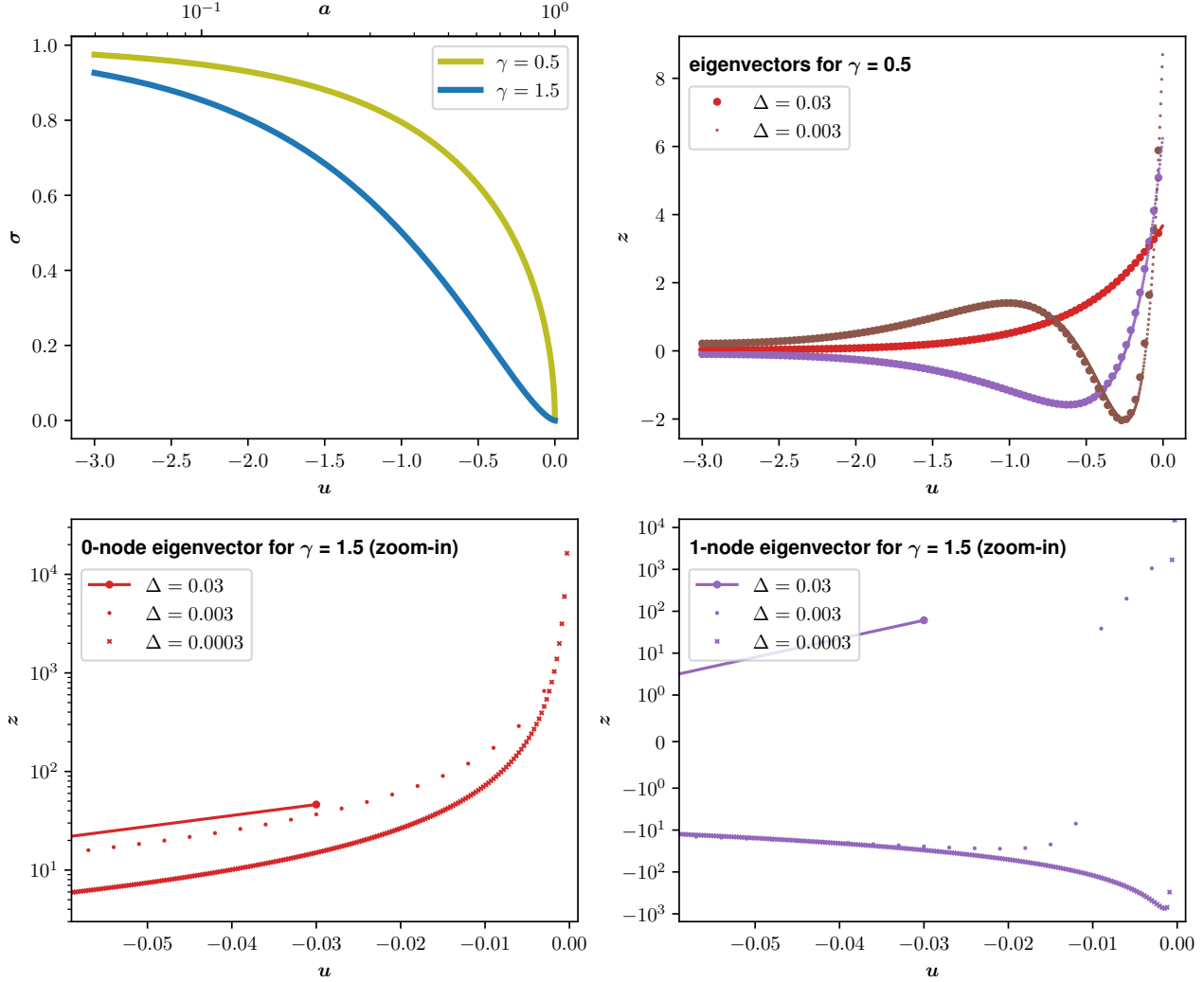


Figure 3. Disk Profiles and Eigenvectors

5. THEORY

The behavior observed in the previous section follows from the dispersion relation. We derive the dispersion relation by adopting the ansatz

$$z = \text{const} \times \frac{1}{\sigma(u)} e^{i(\omega t - ku)} \quad (14)$$

for k assumed constant and real. Aside from the σ prefactor (to be discussed shortly), the spatial dependence is that of a logarithmic spiral: it has constant wavelength in $u \equiv \ln a$ (Binney & Tremaine 2008). The temporal dependence corresponds to the spiral precession at angular frequency ω . We shall find that $\omega > 0$, which implies prograde precession. Inserting this ansatz into the master equation (Equation (6)) gives

$$\frac{\omega}{\sigma(u)} e^{-iku} = \frac{1}{a(u)} \int_{-\infty}^{\infty} \left(K_1 \frac{\sigma(u')}{\sigma(u)} e^{-iku} - K_2 e^{-iku'} \right) du',$$

where we again suppress the dependence of the K 's on $u' - u$ for clarity. Multiplying through by e^{iku} and replacing $K_2 e^{ik(u-u')} \rightarrow K_2 \cos(k(u' - u))$ due to the symmetry of K_2 , we arrive at the dispersion relation

$$\omega(k, u) = \frac{\sigma(u)}{a(u)} \mathcal{K}(k) + \nu(u) \quad (15)$$

where

$$\mathcal{K}(k) \equiv 2 \int_0^{\infty} K_2(v) (1 - \cos kv) dv \quad (16)$$

$$\nu(u) \equiv \frac{1}{a(u)} \int_{-\infty}^{\infty} (K_1 \sigma(u') - K_2 \sigma(u)) du' \quad (17)$$

We have added a K_2 term to Equation (16) and subtracted it from Equation (17) in order to ensure that \mathcal{K} and ν are each finite. We call $\nu(u)$ the precession rate, because it will be seen to be equal to ω at a mode's turning point. Tremaine (2001) defines the precession

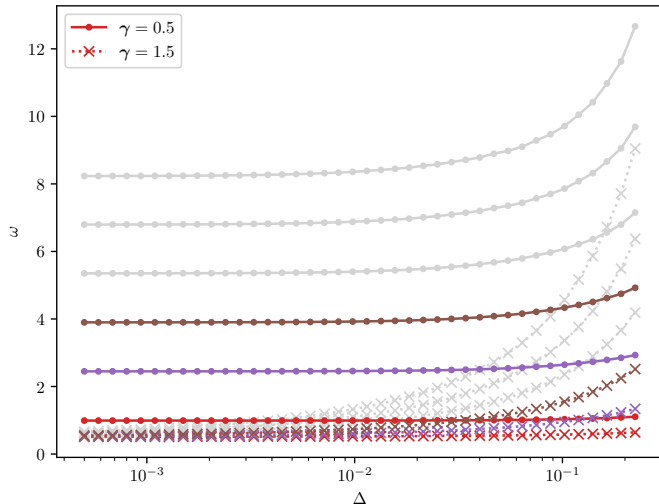


Figure 4. Eigenvalues (mode frequencies) vs. grid spacing: For each profile ($\gamma = 0.5$ and 1.5), the first 6 eigenvalues are shown. For the $\gamma = 0.5$ case, the eigenvalues are well separated at high resolution. But for the $\gamma = 1.5$ case, they become degenerate at high resolution.

rate differently, as just the K_1 term in Equation (17), or equivalently as the coefficient of iz in the master equation. That expression diverges if the softening is strictly zero.⁹

The above dispersion relation is very simple, in that there are no complex numbers, and its dependencies on k and u are clearly separated. It is an exact consequence of the master equation, subject only to the assumptions that k be constant and real.¹⁰ Unlike in WKB theory, one need not assume that $|k|$ be large. A different dispersion relation is derived in Lee et al. (2019a) by expanding the equation of motion at large k , to $O(1/k^2)$. But Equation (15) is both simpler and valid at any k . The simplicity relies on two “tricks” that are standard in galactic dynamics (Kalnajs 1971): (i) the kernels are expressed as a function only of the difference of independent variables ($u' - u$), and (ii) σ is factored out of the exponential ansatz (Equation (14)). But unlike what is often done in galactic dynamics (e.g., Zang 1976; Bertin & Mark 1979; Evans & Read 1998), we do not make any assumptions regarding the shape of the background surface density profile $\sigma(u)$. That allows us to avoid the cumbersome “Kalnajs kernel” $K(\alpha, m = 1)$, which is related to the Fourier transform of our $K_m(v)$.

⁹ Though it converges in the limit that the softening parameter approaches, but does not actually reach, zero.

¹⁰ When we apply the dispersion relation below, we will violate the assumption that k be constant, in effect assuming that it is nearly constant.

The function $\mathcal{K}(k)$ in the dispersion relation is a universal function of k , independent of σ . It is plotted in Figure 6. Its behavior at $|k| \gg 1$ is obtained by replacing $K_2(v) \rightarrow 1/(\pi v^2)$ (Equation (7)), in which case $\mathcal{K} \rightarrow |k|$. Hence at large $|k|$,

$$\omega \approx \frac{\sigma}{a}|k| + \nu, \quad \text{for } |k| \gg 1 \quad (18)$$

$$= \frac{\pi G \Sigma}{\Omega a}|k| + \nu \quad (19)$$

This is nearly the same as the Lin-Shu dispersion relation, after setting the sound speed to zero, the azimuthal wavenumber $m_\phi = 1$, the epicyclic frequency to Ω , and expanding in ω/Ω . But our expression for ν is different from Lin-Shu, and our k provides the wavelength in u rather than in a (see discussion in Lee et al. 2019a).

Before addressing ν , we may already see why soft edges fail to trap modes. The group velocity is

$$v_{\text{group}} = \frac{\partial \omega}{\partial k} = \frac{\sigma}{a} \frac{d\mathcal{K}}{dk} \quad (20)$$

$$\approx \pm \frac{\sigma}{a}, \quad \text{for } |k| \gg 1 \quad (21)$$

which corresponds to the speed (du/dt) of a wavepacket; the reason for taking the $|k| \gg 1$ limit will be clarified at the end of Section 5.1. The travel time from some initial u_{init} to the edge is

$$T = \int_{u_{\text{init}}}^0 \frac{1}{v_{\text{group}}} du \quad (22)$$

$$\approx \int_{u_{\text{init}}}^0 \frac{a}{\sigma} du. \quad (23)$$

Only for sufficiently sharp edges will this time be finite, indicating that the wavepacket can bounce back from the edge. Hunter & Toomre (1969) explain this result in a slightly different way: they show that the number of nodes is infinite when the integral in Equation (23) diverges. For our fiducial profile (Equation (12)), we have

$$T \approx \int_{u_{\text{init}}}^0 \frac{du}{|u|^\gamma} \quad (24)$$

after setting $\sigma \approx |u|^\gamma$ and $a \approx 1$, which hold near the edge. Hence the time to reach the edge is finite only when $\gamma < 1$, and only such profiles can support an eccentric mode.

5.1. Energy-level diagrams

The dispersion relation controls more than just the behavior near the edge. It also dictates where eccentric modes exist, how they are trapped, and their eigenfrequencies. We may see that graphically by adopting the technique of energy-level diagrams from quantum mechanics (Teyssandier & Ogilvie 2016; Lee et al.

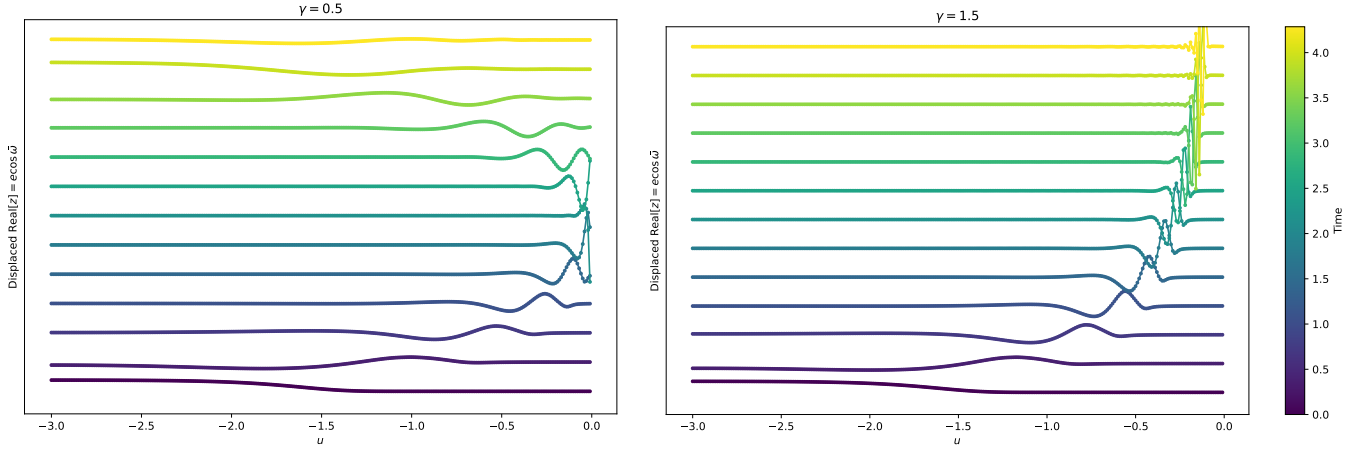


Figure 5. Time evolution: For the $\gamma = 0.5$ case, the disturbance initially travels outward, and then bounces off of the outer edge. For $\gamma = 1.5$, it never reaches the outer boundary, and instead becomes highly oscillatory.

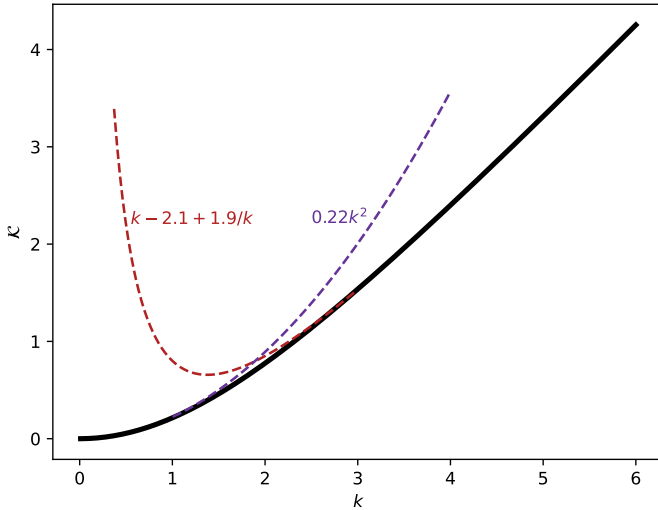


Figure 6. Function $\mathcal{K}(k)$ in Dispersion Relation: The black curve shows $\mathcal{K}(k)$ (Equation (16)). We only show $k > 0$ because it is symmetric, $\mathcal{K}(k) = \mathcal{K}(-k)$. The dashed curves show its approximate form at high and low k . The leading term in the high k expansion ($\mathcal{K} \approx |k|$) is derived in the text, and the subdominant terms have been obtained by numerical integration. For $|k| \ll 1$, one may replace $1 - \cos kv \rightarrow (kv)^2/2$, which produces $\mathcal{K} \approx 0.223k^2$.

2019a). As a reminder of the technique, we first write the Schrödinger equation in a form that parallels Equation (15):

$$E = -\frac{\hbar^2}{2m} \frac{1}{\psi} \frac{d^2\psi}{du^2} + V(u), \quad (25)$$

where the symbols here have their usual quantum-mechanical interpretation. One may solve this equa-

tion for $\psi(u)$ in a bound state, and for the energy E of the bound state. In a given state, $\psi(u)$ is confined by turning points (i.e., inflection points), which occur where $V = E$. In the bound region, where $V < E$, the solution is oscillatory (the squared wavenumber $k^2 \equiv -(1/\psi)d^2\psi/du^2 > 0$), while in the unbound region ($V > E$) it is evanescent. To make the correspondence with eccentric modes, the independent variables are related via

$$\psi \leftrightarrow \sigma z, \quad (26)$$

because Equation (14) implies $k^2 = -1/(\sigma z)d^2(\sigma z)/du^2$. And comparing Equation (25) with Equation (15), we see the further correspondences

$$E \leftrightarrow \omega \quad (27)$$

$$V \leftrightarrow \nu \quad (28)$$

$$-\frac{\hbar^2}{2m} \frac{1}{\psi} \frac{d^2\psi}{du^2} \leftrightarrow \frac{\sigma}{a} \mathcal{K}(k). \quad (29)$$

The last correspondence is not perfect, both because of the u -dependent prefactor (σ/a), and because $\mathcal{K} \propto k^2$ holds only at low $|k|$ (Figure 6). But that imperfection does not affect the most important quantity extracted from an energy level diagram: the location of the turning points, i.e., where $k = 0$. In particular, one may plot the “potential” $\nu(u)$, and consider what happens for different “energies” ω . Eccentric modes will be trapped by the turning points which occur where $\omega = \nu$. The sign of $\omega - \nu$ dictates whether the “wavefunction” σz is evanescent or oscillatory.

We now apply the technique to the two fiducial profiles studied in Section 4. In Figure 7, we show their effective potentials, $\nu(u)$. For the sharp edge (yellow), ν rises

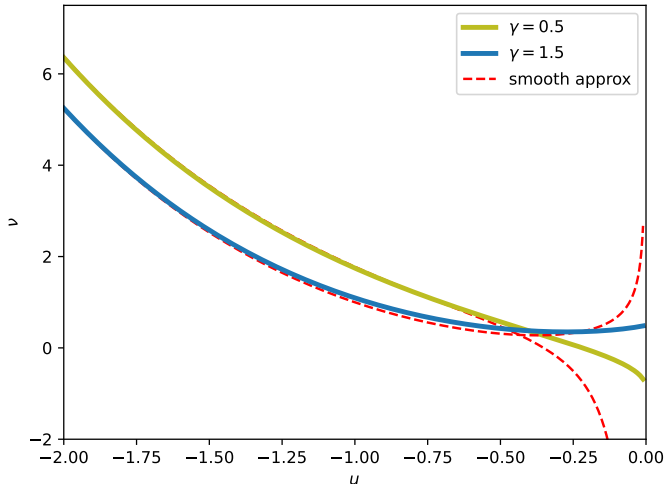


Figure 7. Precession rates in our two fiducial profiles: The precession rate is defined in Equation (17). The “smooth approximation” is from Taylor-expanding σ in Equation (17) to $O(u - u')^2$, which yields $\nu \approx \frac{1}{a} (0.96\sigma + 0.37d^2\sigma/du^2)$. It is inaccurate near the edge, because σ varies too rapidly there.

inwards, showing that a mode must be confined to the outermost parts of the disk—it behaves as an edge mode. For the soft edge (blue), there is a shallow potential well slightly interior to the edge. We also show in the figure a simple approximation to ν , which provides an adequate approximation everywhere except near the edge.

Figure 8 (top panel) shows the energy-level diagram for the sharp-edge case. The function $\nu(u)$ there is repeated from Figure 7, and the horizontal lines show the frequencies of the first three modes, shown previously in Figure 4. To illustrate that the turning points occur where $\nu = \omega$, we re-plot the eigenfunctions (shown previously in Figure 3), but now premultiplied by σ because of Equation (26). It may be seen that the crossing points in the top panel occur at the same place as the inflection points in the middle one.

The bottom panel shows a “dispersion relation map,” which provides a complementary view to the top panel (e.g. Binney & Tremaine 2008; Tremaine 2001; Lee et al. 2019a). Here the function $\omega(k, u)$ is displayed as a contour map. The three colored curves have the same values of ω as the first three eigenfunctions that appear in the top panels. Each of those curves is the “train track” along which the corresponding mode is confined.

The question of what happens near the outer edge is answered by the shape of these curves near the right boundary. The shape is determined by $\omega \approx |u|^\gamma |k|$, which follows from the dispersion relation at large $|k|$. For a contour to represent a mode, one needs the area

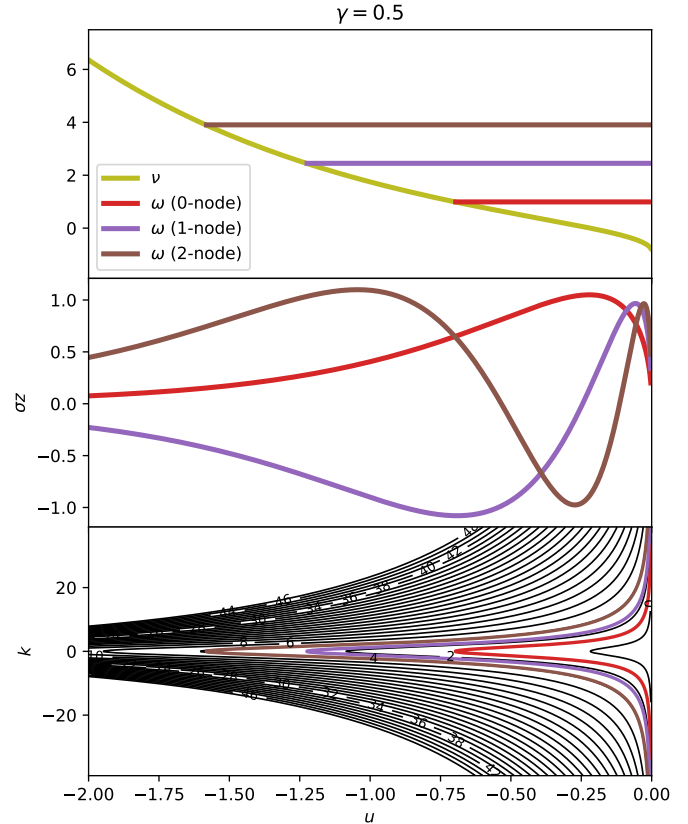


Figure 8. Mode trapping in sharp-edged disk: The top panel shows the energy level diagram; the middle panel shows the eigenfunctions (scaled by σ); and the bottom panel shows the dispersion relation map.

enclosed by the contour to be $\oint k du = \pi, 3\pi, 5\pi, \dots$ (Lee et al. 2019a). Hence with $k \propto |u|^{-\gamma} = |u|^{-0.5}$, the area within any of the contours is finite, leading to well-separated frequencies. The case $\gamma = 1.5$ will lead to the opposite conclusion. One may see also from this panel that our earlier assumption that $|k| \gg 1$ near the edge (Equation (21)) is justified.

Figure 9 shows what happens for the $\gamma = 1.5$ case. The eigenvalues and eigenvectors shown here are calculated with $\Delta = 0.001$. From the bottom panel, one sees that the colored contours near the outer boundary are much steeper than for the $\gamma = 0.5$ case. As explained above, these here have functional form $k \propto |u|^{-1.5}$, and so the area enclosed by those contours, $\oint k du$, does not converge.

6. OTHER DISK PROFILES

We examine the eccentricity solutions for two additional kinds of density profiles. For the first kind, we examine the role of an inner edge. We take $\sigma(u)$ to be the same as our fiducial profile with a sharp edge

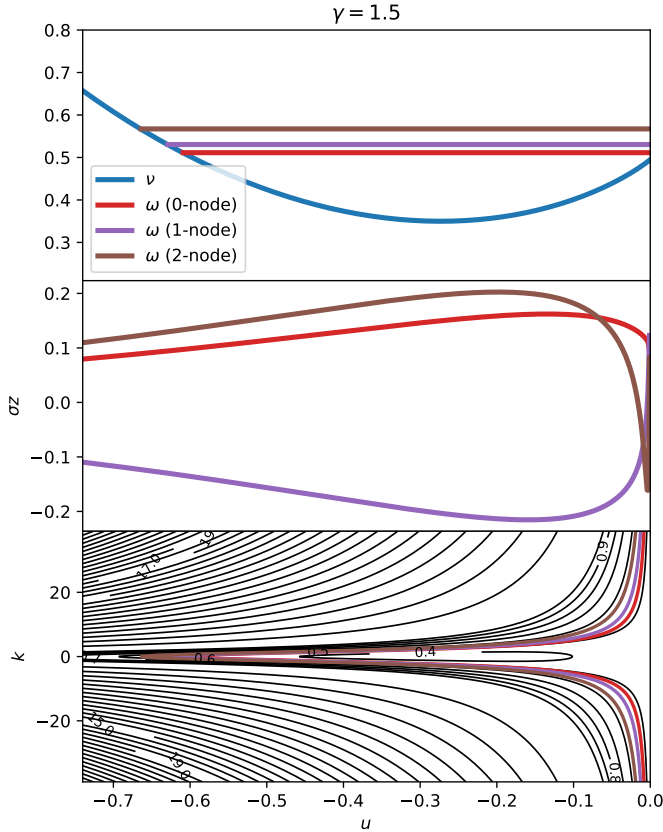


Figure 9. Mode Trapping in Soft-Edged Disk.

($\gamma = 0.5$, Equation (12)), but now we sharply truncate σ to zero at an inner edge. The top panel of Figure 10 shows the four σ profiles considered, which differ in the location of the inner edge. In the bottom two panels, we show the resulting eigenvalues and eigenvectors for the zero-node mode. We see that once the inner edge is at $u_{\text{edge}} \lesssim -1.5$, the eigensolution is independent of the edge's location, as previously claimed. The reason for this independence is that the eccentricity mode is an edge mode. From the energy-level diagram (middle panel), it is trapped between the outer edge and where the effective potential ν intersects ω .¹¹

For the second case, we consider a narrow Gaussian ring,

$$\sigma = e^{-\frac{u^2}{2s^2}}. \quad (30)$$

Tremaine (2001) finds that a Gaussian ring can support eccentric modes, provided it is sufficiently narrow

¹¹ Calling the mode an edge mode does not imply the σz profile in the evanescent zone is irrelevant. Each eigensolution is a global solution; the σz profile everywhere matters, but less for σz farther from the oscillatory zone.

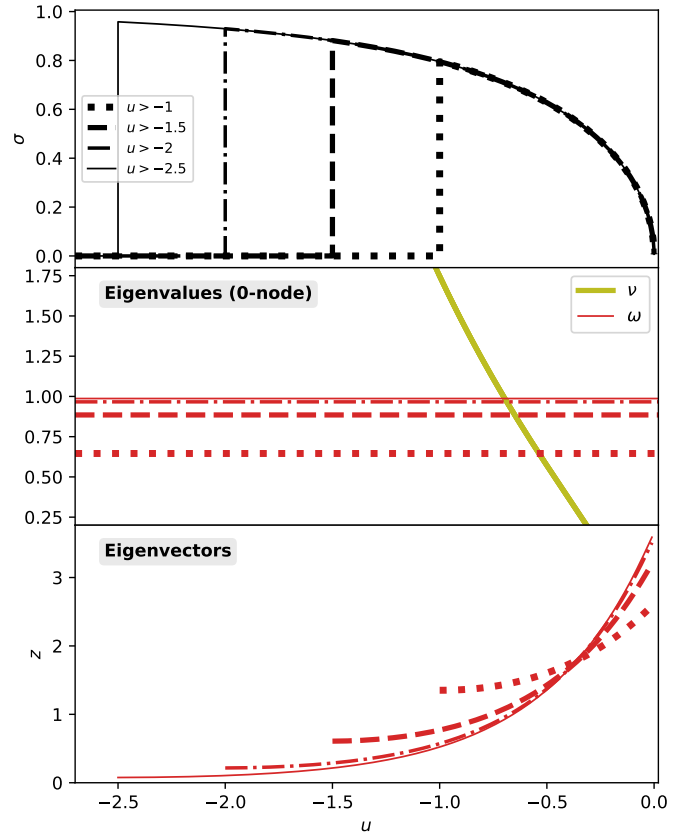


Figure 10. Effect of Inner Edge: The top panel shows four $\sigma(u)$ profiles. They are the same as the previous sharp edge case ($\gamma = 0.5$), but here truncated at an inner edge. The middle panel shows the effective potential ν , and the eigenvalues ω of the 0-node in each of the four profiles, similar to the top panel of Figure 8, but zoomed in. The bottom panel shows the four corresponding eigenvectors; unlike in Figure 8, the eigenvectors are not scaled here by σ .

($s < 0.07$). But that result, taken at face value, contradicts our finding that a mode can only be supported if the integral $\int (a/\sigma) du$ converges (Equation (23)). For a Gaussian ring the integral diverges, whatever the value of s . The apparent contradiction is resolved by noting that the numerical experiments of Tremaine (2001) restrict $|u| < 5s$, in effect adding a sharp truncation at $|u| = 5s$. To illustrate, we show in Figure 11 the result from a σ profile that is equivalent to the one in Tremaine, with $s = 0.05$ and $|u|$ truncated at $5s$ (i.e., $|u| < 0.25$). For that case, Tremaine finds a well-behaved mode. The green curve in the top panel is the σ profile, and the one in the bottom panel is our resulting zero-node eigenvector, σz . We have confirmed that the shape of z is

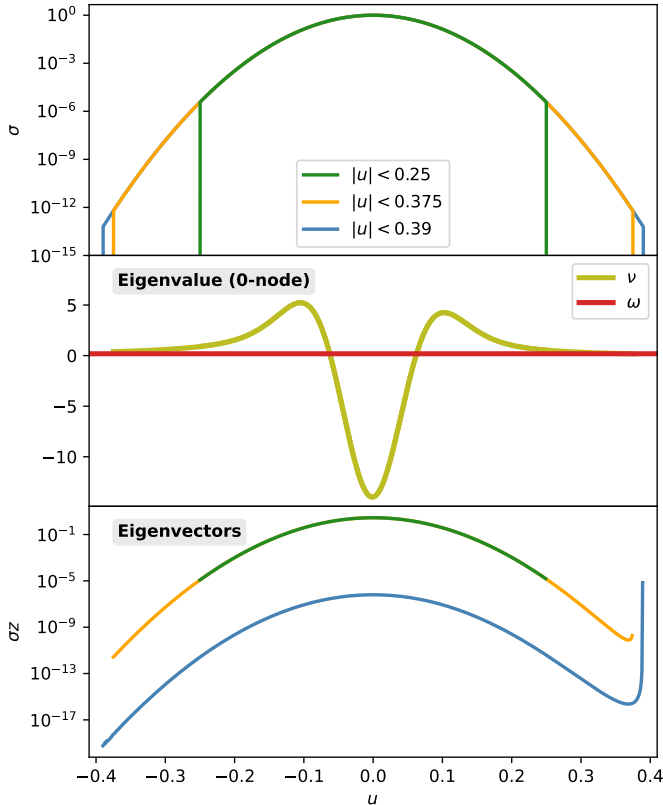


Figure 11. Truncated Gaussian Ring: The top panel shows three Gaussian $\sigma(u)$ profiles with scale $s = 0.05$ (Equation (30)), and truncated at $|u| = 0.25, 0.375,$ and 0.39 . The first truncation is equivalent to that in Tremaine (2001). The middle panel shows the energy-level diagram; the ν and ω for all three truncations are plotted, but the differences are too small to see. The bottom panel shows the zero-node eigenvectors for each of the three σ profiles. This figure is made with resolution $\Delta = 0.001$, but we have confirmed that for smaller Δ there is no visible change.

the same as his. We also show in the figure what happens when we increase the truncation to $|u| = 0.375$ and then 0.39 : the eigenvector shoots up dramatically near the outer boundary. Recalling that our eigenvectors are normalized to unit AMD, we see that at a truncation of 0.39 , the AMD is dominated near the outer boundary. When the truncation is increased beyond 0.39 by a very small amount, the eigenvector continues its extremely rapid rise, indicating that the eigenvector is pathological. Hence an untruncated Gaussian ring cannot support linear modes.

7. DISCUSSION

7.1. Neglected Effects

We showed that self-gravitating disks can only sustain an eccentricity if they have a sufficiently sharp edge; in particular, the edge must be sufficiently sharp that $\int da/\sigma$ converges at the edge (Equation 23). To derive this result, we assumed that the disk is 2D, is forced solely by gravity, and is governed by linear secular theory. Most or all of these assumptions must be relaxed in realistic disks. Nonetheless, the dynamics discussed here should provide a foundation for understanding more realistic disks. Some of the most important additional effects are as follows:

- **Pressure:** For eccentric modes in a fluid disk, the strength of pressure relative to self-gravity is quantified by the dimensionless parameter h^2/μ , where $h = (c/\Omega a)$, c is the sound speed, and μ is the local ratio of disk mass to central body mass (Lee & Goodman 1999; Lee et al. 2019a). Self-gravity dominates when

$$\mu \gtrsim h^2 \quad (\text{strong gravity}). \quad (31)$$

In terms of Toomre’s stability parameter, $Q \sim h/\mu$, that requirement reads

$$Q \lesssim 1/h \quad (32)$$

Disk stability adds an additional requirement, $Q \gtrsim 1$ (i.e., $\mu \lesssim h$). Disks in the weak-gravity limit ($\mu \lesssim h^2$) support purely pressure-dominated modes, and the trapping of such modes is much less sensitive to the disk’s outer profile (e.g., Lee et al. 2019b).¹² Lee et al. (2019a) study disks with pressure and self-gravity in both weak- and strong-gravity regimes, where the disks have soft edges.

¹² The difference between gravity and pressure dominated disks can be seen from the functional form of the dispersion relation $\omega(k, u)$, graphically depicted as contours in the dispersion relation map (DRM). Those contours are the train tracks along which a mode travels. For gravity-dominated modes the contours have a hyperbolic-like shape at the outer edge (Figure 8, bottom panel), and so a mode travelling outward does not turn back until it reaches the edge. Equivalently, reflection requires zero group velocity, and since the group velocity is $\propto \Sigma$ at high k (Equation (21)), reflection requires $\Sigma = 0$ (reached either continuously, as in the σ profile of Equation (12), or discontinuously, as in the step-function surface densities considered by Sridhar et al. 1999). By contrast, for pressure-dominated modes the contours in the DRM are ellipses centered on the $k = 0$ axis (see Figure 5, top-left panel, in Lee et al. 2019a). In following an ellipse, an outwardly travelling mode turns back before reaching the edge. From the group velocity, which is $-h^2\Omega k$ in the pressure case, one may also infer that reflection occurs at $k = 0$ (the Lindblad resonance; Lee et al. 2019a).

They find trapped pressure modes in the weak-gravity regime, and no modes (or more precisely, pathological very-small-wavelength modes) in the very-strong-gravity regime, consistent with the results of the present paper and Lee et al. (2019b). Were Lee et al. (2019a) extended to model sharp edges, the disks would presumably support large wavelength eccentric modes whether gravity was in the weak or strong limit.

- Finite thickness, random velocities, and softening: Hahn (2003) models the finite thickness of a disk with softening. Since softening acts somewhat like pressure (Tremaine 2001), one might expect that the same considerations discussed above for pressure would apply here, but with h now representing the disk’s aspect ratio. Non-fluid disks, such as stellar disks in galactic centers or debris disks, could behave similarly, as they have scale-height $\sim v_{\text{random}}/\Omega$. Softening can also be used to treat cases where orbits cross, e.g., to obtain precession rates of orbit-crossing test particles embedded in disks.
- External potential: It would be of interest to extend the study in the present paper to include an external potential, which might help trap an eccentric mode, even if the disk has a soft edge. In protoplanetary disks or planetary rings, the external potential would typically come from a companion (planet or moon), or a bulge on the central body. Tremaine (2001) includes externally-driven precession, which indeed helps traps his modes. But for simplicity he does not model a companion’s potential. Instead, he scales the K_1 term in our master equation (Eq. 6) by a constant factor.

Tremaine finds that some of his modes have negative eigenfrequencies, whereas Laplace-Lagrange (L-L) theory should always produce positive eigenfrequencies for eccentric modes.¹³ He argues on this basis that L-L does not give the correct answer for a continuous disk. We contend that L-L is correct (see the end of our section 2), and that it is his external precession that is the source of the negative eigenfrequencies. To be specific, his external precession is equivalent to that from a “frozen” (time-independent) potential of an axisymmetric disk having a scaled version of our disk’s surface density profile. Thus his setup requires orbits in

the eccentric disk to cross those in the frozen circular disk. It is that orbit-crossing that makes L-L invalid, and the eigenfrequencies negative.

- Nonlinearity: In disks with a soft edge, an eccentric disturbance becomes nonlinear as it leaks into the low density region (Figure 5, right panel). In order to find out what happens next, one must include nonlinear effects. Lee & Goodman (1999) study the nonlinear dynamics of forced eccentric modes in power-law disks.
- Excitation and Decay: Even if a disk can sustain eccentric modes, that does not guarantee that it is eccentric. There must additionally be a mechanism to excite the eccentricity. One possibility for excitation is a companion such as a planet or binary star. A second is instability. The indirect potential can lead to instability for sufficiently massive disks, even if the disk is Toomre-stable (Adams et al. 1989; Shu et al. 1990). Instability can also be triggered by a locally isothermal equation of state (Lin 2015), by a finite cooling time (Li et al. 2021), or by non-axisymmetric irradiation (“shadows”) (Qian & Wu 2024).

After an eccentric mode is excited, it can be damped by viscosity. Pressure-dominated modes are relatively immune to viscous damping: their decay time is comparable to the viscous time of the disk (Teyssandier & Ogilvie 2016; Lee et al. 2019b), which should be comparable to the disk’s lifetime. The viscous decay time for self-gravity-dominated modes is likely also long.

- Warped disks with self-gravity: the governing equation for a warped disk is nearly identical to our master equation (Equation 6). The only differences are that z in that equation should represent the complex inclination ($z \rightarrow ie^{i\Omega}$ in standard notation) rather than the complex eccentricity, and one must replace $K_2 \rightarrow K_1$ (Murray & Dermott 1999). Hence our dispersion relation and analysis carries through virtually unchanged. Batygin (2018) investigates warped disks with self-gravity by adopting a number of simplifications. He considers a profile with $\sigma/a = \text{const}$, and approximates self-gravity by considering only nearest-neighbor interactions. His resulting dispersion relation is $\omega = \text{const} \times k^2$ (his Equation 33), which is the same as for the potential-free Schrödinger equation. Contrasting his dispersion relation with ours (Equation 15), we see that his corresponds to dropping the ν term, and taking the small k limit

¹³ For an inclined (warped) disk, L-L eigenfrequencies are negative.

of $\mathcal{K}(k)$. Such an approximation may be justifiable under specific conditions.

7.2. Potential Applications

- **Protoplanetary Disks:** Some protoplanetary disks have eccentric dust cavities, including MWC 758 and AB Aur (Dong et al. 2018; van der Marel et al. 2021), and others (Jensen et al. 2024). A standard explanation for the origin of the eccentricity is a massive planet, which can excite the disk’s eccentricity when the planet is more than a few Jupiter masses (Papaloizou et al. 2001; Kley & Dirksen 2006; Dempsey et al. 2021), although other explanations have also been proposed (e.g., Qian & Wu 2024). Some young (Class 0) disks exhibit asymmetry (Thieme et al. 2023; van’t Hoff et al. 2023), which has been attributed to disk eccentricity instigated by non-axisymmetric accretion during cloud collapse (Commerçon et al. 2024).

Many protoplanetary disks are sufficiently massive that self-gravity dominates pressure for the dynamics of the eccentric modes (Equation 32). We would expect that such disks could only be eccentric if their edges were extremely sharp. However, multiple effects not considered here could alter that conclusion, including nonlinearity and the relative of importance of pressure and self-gravity near the edge (Section 7.1). Those effects must be addressed before making definite predictions.

- **Planetary Rings:** Uranus’s ϵ ring is eccentric, despite differential precession from Uranus’s quadrupole which would quickly destroy the eccentricity in the absence of a counterbalancing force. Goldreich & Tremaine (1979a) proposed that the eccentricity can be maintained by self-gravity. Other rings (e.g., the Uranian α and β rings, and Saturn’s Maxwell ring) have broadly similar properties. The ϵ ring is observed to have sharp edges, which are maintained by the shepherd moons Cordelia and Ophelia (Goldreich & Tremaine 1979b; Borderies et al. 1982, 1989; Porco & Goldreich 1987; Goldreich & Porco 1987), and it and other rings lie in the strong gravity regime by a large margin ($Q \sim 1$ and $h \ll 10^{-6}$; see Equation 32). Plausibly, sharp edges are essential for these rings to maintain their eccentricities. However, some of the effects neglected in this paper play important roles in narrow eccentric rings, including nonlinearity and pressure. Nonlinearity is included in the model of Goldreich &

Tremaine (1979a), and the same nonlinear equations are modified by pressure forces in the model by Chiang & Goldreich (2000). The latter authors showed that pressure forcing, which is especially strong near ring edges, is needed to quantitatively account for the measured eccentricities and masses of the Uranian rings. See also Chiang & Culter (2003) who extended these considerations to treat inclinations.

- **Stellar Disks in Galactic Nuclei:** M31 has a double nucleus that can be explained as an eccentric disk of stars (Tremaine 1995). A variety of other galaxies also host double nuclei (Lauer et al. 1996; Thatte et al. 2000; Debattista et al. 2006). As discussed above, Sridhar et al. (1999) modelled eccentric nuclear disks with Laplace-Lagrange theory. They adopted power-law surface density profiles with infinitely sharp edges, and they successfully found eccentric modes. That result is understandable from our theory. Observationally, M31 has an aspect ratio $h \sim 0.4$, and a ratio of disk to black hole mass of $\mu \sim 0.15$ (Peiris & Tremaine 2003). Thus from Equation (31), the effect of finite scale height may be important.

8. SUMMARY

A Keplerian disk in the strong-gravity regime ($\mu \gtrsim h^2$) must have a sharply truncated edge in order to be eccentric. The surface density Σ must hit zero at the edge, and the integral in Equation (23) must converge, which means that the time for a wavepacket to reach the edge must be finite. We may approximate that requirement as

$$\int^{a_{\text{edge}}} \frac{da}{\Sigma(a)} < \infty. \quad (33)$$

Asymptotic outer edges, e.g., of the form $\Sigma \sim e^{-a^\xi}$ for any ξ , are insufficiently sharp to support an eccentric mode. Hunter & Toomre (1969) similarly show that the integral in Equation (33) must converge in order for a galactic disk to support a warp. They draw an analogy with waves on a lake, which last much longer when the lake is bounded by vertical cliffs than by beaches. That is because waves are reflected by cliffs but not beaches. For a disk with a sufficiently sharp edge, the wave is reflected by the edge, whereas if the edge is soft the eccentric disturbance leaks out into the edge region, and its energy (or really, AMD) is lost.

For our fiducial sharp profile (Equation (12) with $\gamma = 0.5$), the normal modes are edge modes. Their AMD is dominated near the outer boundary, and the

trapping zone is within less than a decade of the edge (Figure 8, top panel). For different surface density profiles, the modes' AMD can be dominated at the inner edge (Sridhar et al. 1999), in which case Equation (33) should apply at the inner edge.

We also showed that two-dimensional disks supported by self-gravity may be analyzed without introducing artificial softening. Nonetheless, softening may still be useful as a model for additional effects such as pressure or a finite vertical extent (Tremaine 2001; Hahn 2003). In the appendix, we derived a discretized equation for the eccentricity that does not use softening, conserves a discretized AMD, and converges rapidly with grid spacing (Equation (A15)). Some previous studies have introduced softening-free algorithms (Laughlin & Korchagin 1996; Lee et al. 2019a). But the algorithm in Equation (A15) is more straightforward to implement, and we have verified that its accuracy is $O(\Delta^2)$ (Figure 2).

Finally, we derived a new and simple dispersion relation for eccentric disturbances (Equation (15)). Un-

like WKB, it is valid at any wavenumber. It allows one to show that the integral of Equation (33) controls the travel time to the edge. More generally, it allows one to plot energy-level diagrams that are familiar from solving Schrödinger's equation. The diagrams provide a graphical depiction of where eccentric modes are trapped, and of their precession frequencies.

ACKNOWLEDGEMENTS

We thank Scott Tremaine for insightful and detailed feedback on this work and for telling us about Hunter & Toomre (1969). We also thank an anonymous referee for a constructive report and Antranik Sefilian for helpful pointers to the literature on softening and eccentric modes. Y.L. acknowledges NASA grant 80NSSC23K1262. E.C. acknowledges a Simons Investigator grant, a Berkeley Discover grant for undergraduate education, and a Berkeley Letters & Science Summer Undergraduate Research Fellowship (SURF) awarded to Z.Y.

APPENDIX

A. DISCRETIZATION

We write the master equation (Equation (6)) as

$$\dot{z} = i \frac{1}{a} \mathcal{I}(u) , \quad (\text{A1})$$

where

$$\mathcal{I}(u) \equiv \int (K_1 z - K_2 z') \sigma' du' \quad (\text{A2})$$

and discretize \mathcal{I} on a grid in u . The spacing in u is taken to be uniform, and denoted Δ . For the purposes of the derivation, we imagine that z and σ are smooth functions of u , and that their values on the grid are known. Gridpoints are labelled u_j , for integer j , and the values of z and σ on the grid are z_j and σ_j .

As explained in the body of the paper, the $K_m \equiv K_m(u - u')$ diverge as u' approaches u . But \mathcal{I} remains finite, despite that divergence, because as $u' \rightarrow u$, then both $z' \approx z$ and $K_2 \approx K_1$. To separate out those two effects, we first decompose

$$\mathcal{I} = \mathcal{A} + \mathcal{B} \quad (\text{A3})$$

$$\mathcal{A} = \int K_2 (z - z') \sigma' du' \quad (\text{A4})$$

$$\mathcal{B} = z \int (K_1 - K_2) \sigma' du' \quad (\text{A5})$$

and discretize each of the components \mathcal{A} and \mathcal{B} in turn.

The naive discretization of $\mathcal{A}_j \equiv \mathcal{A}(u_j)$ is, in obvious notation,

$$\mathcal{A}_j^{\text{naive}} = \Delta \sum_{k \neq j} K_{2,jk} (z_j - z_k) \sigma_k \quad (\text{A6})$$

But one must be careful at the gridpoint $k = j$, since K_2 diverges there, while $z_j - z_k$ vanishes. In the naive method in Equation (A6), we simply discarded the $k = j$ point. To examine whether that is sufficiently accurate, we write the

contribution to $\mathcal{A}(u)$ within a distance $\Delta/2$ as

$$\mathcal{A}^\Delta(u) = \int_{-\Delta/2}^{\Delta/2} K_2(v)(z - z_+) \sigma_+ dv \quad (\text{A7})$$

$$= \int_0^{\Delta/2} K_2(v) [(z - z_+) \sigma_+ + (z - z_-) \sigma_-] dv \quad (\text{A8})$$

where in the first line we changed the integration variable to $v \equiv u' - u$, and defined $z_+ = z(u + v)$, and similarly $\sigma_+ = \sigma(u + v)$; and in the second line we combined positive and negative values of v , taking advantage of the symmetry of K_2 , and defined $z_- = z(u - v)$, and similarly for σ_- . As we are concerned presently with small Δ , we Taylor-expand the integrand in v , which gives

$$\mathcal{A}^\Delta(u) \approx \left[z \frac{d^2}{du^2} \sigma - \frac{d^2}{du^2} (z\sigma) \right] \int_0^{\Delta/2} K_2(v) v^2 dv . \quad (\text{A9})$$

Since $K_2(v) \propto 1/v^2$ at small v , the integral in that expression converges. But the integrand is flat in v , and thus discarding the $k = j$ contribution to Equation (A6) leads to a fractional error of $\sim \Delta$. That is indeed small; but one can do better. One can correct the leading error in a nearly trivial way by changing the discretization from Equation (A6) to

$$\mathcal{A}_j = \Delta \sum_k K_{2,jk} (z_j - z_k) \sigma_k F_{jk} , \quad (\text{A10})$$

where

$$F_{jk} = \begin{cases} 0 & \text{if } k = j, \\ 1.5 & \text{if } k = j \pm 1, \\ 1 & \text{otherwise.} \end{cases} \quad (\text{A11})$$

The factor of 1.5 compensates for the discarded $k = j$ term, taking advantage of the fact that the integrand is nearly independent of v . The error in the discretization is now $\sim \Delta^2$, as confirmed experimentally in the body of the paper.

Next, we turn to \mathcal{B} (Equation (A5)), which we discretize as follows

$$\mathcal{B}_j = z_j \Delta \sum_k L_{jk} \sigma_k \quad (\text{A12})$$

where

$$L_{jk} = \frac{1}{\Delta} \int_{u_k - u_j - \Delta/2}^{u_k - u_j + \Delta/2} (K_1(v) - K_2(v)) dv . \quad (\text{A13})$$

These integrals are precomputed numerically. For the diagonal component (L_{jj}), the integrand diverges at $v \sim 0$. But the divergence is sufficiently weak ($\sim \ln |v|$) that the integral converges. If the functional form of $\sigma(a)$ is known, one could alternatively integrate Equation (A5) exactly, i.e., without pulling the σ' out of the integral. But the increased accuracy is of little benefit, as we have already discretized σ for \mathcal{A} .

Collecting results, we have shown that the integral \mathcal{I} , as defined in Equation (A2), is to be discretized as

$$\mathcal{I}_{\text{discrete}}(u_j) = \Delta \sum_k K_{2,jk} F_{jk} (z_j - z_k) \sigma_k + z_j L_{jk} \sigma_k \quad (\text{A14})$$

where F_{jk} and L_{jk} are provided by Equations (A11) and (A13). The discretized equation of motion is then

$$\dot{z}_j = i \frac{1}{a_j} \Delta \sum_k K_{2,jk} F_{jk} (z_j - z_k) \sigma_k + z_j L_{jk} \sigma_k \quad (\text{A15})$$

A.1. Matrix Formulation and Eigenvalue Equation

In order to solve Equation (A15) numerically, we convert it to matrix form. We represent z_j as a column vector \mathbf{z} , and similarly for a_j and σ_j :

$$z_j \leftrightarrow \mathbf{z} \quad (\text{A16})$$

$$a_j \leftrightarrow \mathbf{a} \quad (\text{A17})$$

$$\sigma_j \leftrightarrow \boldsymbol{\sigma} . \quad (\text{A18})$$

And we represent $K_{2,jk}F_{jk}$ and L_{jk} as matrices:

$$K_{2,jk}F_{jk} \leftrightarrow \mathbf{K}_2 \quad (\text{A19})$$

$$L_{jk} \leftrightarrow \mathbf{L} \quad (\text{A20})$$

The matrix form of Equation (A15) is then

$$\boldsymbol{\Lambda}_a \dot{\mathbf{z}} = i\Delta (\boldsymbol{\Lambda}_{\mathbf{K}_2\boldsymbol{\sigma} + \mathbf{L}\boldsymbol{\sigma}} - \mathbf{K}_2\boldsymbol{\Lambda}_\sigma) \mathbf{z} , \quad (\text{A21})$$

where we represent a diagonal matrix that has a vector (e.g., \mathbf{a}) on its diagonals as

$$\boldsymbol{\Lambda}_a \equiv \text{DIAG}(\mathbf{a}) \quad (\text{A22})$$

We convert this to a more standard form by multiplying both sides by $\boldsymbol{\Lambda}_\sigma$,

$$\boldsymbol{\Lambda}_\sigma \boldsymbol{\Lambda}_a \dot{\mathbf{z}} = i\Delta (\boldsymbol{\Lambda}_\sigma \boldsymbol{\Lambda}_{\mathbf{K}_2\boldsymbol{\sigma} + \mathbf{L}\boldsymbol{\sigma}} - \boldsymbol{\Lambda}_\sigma \mathbf{K}_2 \boldsymbol{\Lambda}_\sigma) \mathbf{z} . \quad (\text{A23})$$

Now the matrix multiplying \mathbf{z} is real and symmetric, as is the matrix multiplying $\dot{\mathbf{z}}$. One consequence of these symmetries is that the discretized equation can be seen by inspection to exactly conserve a discretized AMD

$$\text{AMD}_{\text{discrete}} \equiv \Delta \mathbf{z}^\dagger \boldsymbol{\Lambda}_\sigma \boldsymbol{\Lambda}_a \mathbf{z} = \Delta \sum_k |z_k|^2 \sigma_k a_k \quad (\text{A24})$$

(compare with Equation (8)).

To obtain the eigensolutions of Equation (A23), we set

$$\mathbf{z} = \hat{\mathbf{z}} e^{i\omega t} , \quad (\text{A25})$$

which gives the eigenvalue equation

$$\omega \boldsymbol{\Lambda}_\sigma \boldsymbol{\Lambda}_a \hat{\mathbf{z}} = \Delta (\boldsymbol{\Lambda}_\sigma \boldsymbol{\Lambda}_{\mathbf{K}_2\boldsymbol{\sigma} + \mathbf{L}\boldsymbol{\sigma}} - \boldsymbol{\Lambda}_\sigma \mathbf{K}_2 \boldsymbol{\Lambda}_\sigma) \hat{\mathbf{z}} . \quad (\text{A26})$$

Because of the aforementioned symmetries of the matrices on the two sides of the equation, the eigenvalues and eigenvectors are real, and the eigenvectors are orthogonal when they sandwich the matrix $\boldsymbol{\Lambda}_\sigma \boldsymbol{\Lambda}_a$ (e.g., Goldstein 1980). To be explicit, if we label different eigenvectors with subscript l and m , then

$$\Delta \hat{\mathbf{z}}_l^\dagger \boldsymbol{\Lambda}_\sigma \boldsymbol{\Lambda}_a \hat{\mathbf{z}}_m = \delta_{lm} \quad (\text{A27})$$

Our insertion of Δ in Equation (A27) is arbitrary. But it is convenient because it sets the normalization convention to be that the discretized AMD in a mode is unity; i.e.,

$$\text{AMD}_{\text{discrete}} \equiv \Delta \sum_k |z_k|^2 \sigma_k a_k = 1 \quad (\text{A28})$$

where z_k are the values of z on the grid, for any mode.

REFERENCES

- Adams, F. C., Ruden, S. P., & Shu, F. H. 1989, ApJ, 347, 959
 Batygin, K. 2018, MNRAS, 475, 5070

- Bertin, G. & Mark, J. W. K. 1979, *SIAM Journal of Applied Mathematics*, 36, 407
- Binney, J. & Tremaine, S. 2008, *Galactic Dynamics: Second Edition*
- Borderies, N., Goldreich, P., & Tremaine, S. 1982, *Nature*, 299, 209
- . 1989, *Icarus*, 80, 344
- Chiang, E. I. & Culter, C. J. 2003, *ApJ*, 599, 675
- Chiang, E. I. & Goldreich, P. 2000, *ApJ*, 540, 1084
- Cohl, H. S. & Tohline, J. E. 1999, *ApJ*, 527, 86
- Commerçon, B., Lovascio, F., Lynch, E., & Ragusa, E. 2024, *A&A*, 689, L9
- Davydenkova, I. & Rafikov, R. R. 2018, *ApJ*, 864, 74
- Debattista, V. P., Ferreras, I., Pasquali, A., Seth, A., De Rijcke, S., & Morelli, L. 2006, *ApJL*, 651, L97
- Dempsey, A. M., Muñoz, D. J., & Lithwick, Y. 2021, *ApJL*, 918, L36
- Dong, R., Liu, S.-y., Eisner, J., Andrews, S., Fung, J., Zhu, Z., Chiang, E., Hashimoto, J., Liu, H. B., Casassus, S., Esposito, T., Hasegawa, Y., Muto, T., Pavlyuchenkov, Y., Wilner, D., Akiyama, E., Tamura, M., & Wisniewski, J. 2018, *ApJ*, 860, 124
- Evans, N. W. & Read, J. C. A. 1998, *MNRAS*, 300, 83
- Goldreich, P. & Porco, C. C. 1987, *AJ*, 93, 730
- Goldreich, P. & Tremaine, S. 1979a, *AJ*, 84, 1638
- . 1979b, *Nature*, 277, 97
- Goldstein, H. 1980, *Classical Mechanics*, 2nd edn. (Reading, MA: Addison-Wesley)
- Hahn, J. M. 2003, *ApJ*, 595, 531
- Heppenheimer, T. A. 1980, *Icarus*, 41, 76
- Hunter, C. & Toomre, A. 1969, *ApJ*, 155, 747
- Jensen, S. K., Brittain, S. D., Banzatti, A., Najita, J. R., Carr, J. S., Kern, J., Kozdon, J., Zrake, J., & Fung, J. 2024, *AJ*, 167, 115
- Kalnajs, A. J. 1971, *ApJ*, 166, 275
- Kley, W. & Dirksen, G. 2006, *A&A*, 447, 369
- Lauer, T. R., Tremaine, S., Ajhar, E. A., Bender, R., Dressler, A., Faber, S. M., Gebhardt, K., Grillmair, C. J., Kormendy, J., & Richstone, D. 1996, *ApJL*, 471, L79
- Laughlin, G. & Korchagin, V. 1996, *ApJ*, 460, 855
- Lee, E. & Goodman, J. 1999, *MNRAS*, 308, 984
- Lee, W.-K., Dempsey, A. M., & Lithwick, Y. 2019a, *ApJ*, 872, 184
- . 2019b, *ApJL*, 882, L11
- Li, J., Dempsey, A. M., Li, H., & Li, S. 2021, *ApJ*, 910, 79
- Lin, M.-K. 2015, *MNRAS*, 448, 3806
- Murray, C. D. & Dermott, S. F. 1999, *Solar System Dynamics*
- Papaloizou, J. C. B. 2002, *A&A*, 388, 615
- Papaloizou, J. C. B., Nelson, R. P., & Masset, F. 2001, *A&A*, 366, 263
- Peiris, H. V. & Tremaine, S. 2003, *ApJ*, 599, 237
- Porco, C. C. & Goldreich, P. 1987, *AJ*, 93, 724
- Qian, Y. & Wu, Y. 2024, *ApJ*, 976, 5
- Rendon Restrepo, S., Rometsch, T., Ziegler, U., & Gressel, O. 2025, arXiv e-prints, arXiv:2506.10812
- Sefilian, A. A. & Rafikov, R. R. 2019, *MNRAS*, 489, 4176
- Shu, F. H., Tremaine, S., Adams, F. C., & Ruden, S. P. 1990, *ApJ*, 358, 495
- Silsbee, K. & Rafikov, R. R. 2015, *ApJ*, 798, 71
- Sridhar, S., Syer, D., & Touma, J. 1999, in *Astronomical Society of the Pacific Conference Series*, Vol. 160, *Astrophysical Discs - an EC Summer School*, ed. J. A. Sellwood & J. Goodman, 307
- Teyssandier, J. & Lai, D. 2019, *MNRAS*, 490, 4353
- Teyssandier, J. & Ogilvie, G. I. 2016, *MNRAS*, 458, 3221
- Thatte, N., Tecza, M., & Genzel, R. 2000, *A&A*, 364, L47
- Thieme, T. J., Lai, S.-P., Ohashi, N., Tobin, J. J., Jørgensen, J. K., Sai, J. I. C., Aso, Y., Williams, J. P., Yamato, Y., Aikawa, Y., de Gregorio-Monsalvo, I., Han, I., Kwon, W., Lee, C. W., Lee, J.-E., Li, Z.-Y., Lin, Z.-Y. D., Looney, L. W., Narayanan, S., Phuong, N. T., Plunkett, A. L., Santamaría-Miranda, A., Sharma, R., Takakuwa, S., & Yen, H.-W. 2023, *ApJ*, 958, 60
- Touma, J. R. 2002, *MNRAS*, 333, 583
- Tremaine, S. 1995, *AJ*, 110, 628
- . 2001, *AJ*, 121, 1776
- van der Marel, N., Birnstiel, T., Garufi, A., Ragusa, E., Christiaens, V., Price, D. J., Sallum, S., Muley, D., Francis, L., & Dong, R. 2021, *AJ*, 161, 33
- van't Hoff, M. L. R., Tobin, J. J., Li, Z.-Y., Ohashi, N., Jørgensen, J. K., Lin, Z.-Y. D., Aikawa, Y., Aso, Y., de Gregorio-Monsalvo, I., Gavino, S., Han, I., Koch, P. M., Kwon, W., Lee, C. W., Lee, J.-E., Looney, L. W., Narayanan, S., Plunkett, A., Sai, J. I. C., Santamaría-Miranda, A., Sharma, R., Sheehan, P. D., Takakuwa, S., Thieme, T. J., Williams, J. P., Lai, S.-P., Phuong, N. T., & Yen, H.-W. 2023, *ApJ*, 951, 10
- Zang, T. A. 1976, PhD thesis, -